1-1-2012

Synchrotron radiation spectroscopic techniques as tools for the medicinal chemist: microprobe X-Ray fluorescence imaging, X-Ray absorption spectroscopy, and infrared microspectroscopy

Carolyn Therese Dillon
University of Wollongong, carolynd@uow.edu.au

Synchrotron radiation spectroscopic techniques as tools for the medicinal chemist: microprobe X-Ray fluorescence imaging, X-Ray absorption spectroscopy, and infrared microspectroscopy

Abstract

This review updates the recent advances and applications of three prominent synchrotron radiation techniques, microprobe X-ray fluorescence spectroscopy/imaging, X-ray absorption spectroscopy, and infrared microspectroscopy, and highlights how these tools are useful to the medicinal chemist. A brief description of the principles of the techniques is given with emphasis on the advantages of using synchrotron radiation-based instrumentation rather than instruments using typical laboratory radiation sources. This review focuses on several recent applications of these techniques to solve inorganic medicinal chemistry problems, focusing on studies of cellular uptake, distribution, and biotransformation of established and potential therapeutic agents. The importance of using these synchrotron-based techniques to assist the development of, or validate the chemistry behind, drug design is discussed.

Keywords

radiation, spectroscopic, techniques, tools, medicinal, chemist, synchrotron, microprobe, imaging, x, ray, fluorescence, microspectroscopy, infrared, spectroscopy, absorption, CMMB

Disciplines

Life Sciences | Physical Sciences and Mathematics | Social and Behavioral Sciences

Publication Details

Dillon, C. Therese. (2012). Synchrotron radiation spectroscopic techniques as tools for the medicinal chemist: microprobe X-Ray fluorescence imaging, X-Ray absorption spectroscopy, and infrared microspectroscopy. Australian Journal of Chemistry: an international journal for chemical science, 65 (3), 204-217.

Synchrotron Radiation Spectroscopic Techniques as Tools for the Medicinal Chemist: Microprobe X-Ray Fluorescence Imaging, X-Ray Absorption Spectroscopy and Infrared Microspectroscopy.

Carolyn Therese Dillon

Centre for Medicinal Chemistry

School of Chemistry

University of Wollongong, NSW, 2522

Email: carolynd@uow.edu.au

Abstract

This review updates the recent advances and applications of three prominent synchrotron radiation techniques, microprobe X-ray fluorescent spectroscopy/imaging, X-ray absorption spectroscopy and infrared microspectroscopy, and highlights how these tools are useful to the medicinal chemist. A brief description of the principles of the techniques is given with emphasis on the advantages of using synchrotron radiation-based instrumentation rather than instruments using typical laboratory radiation sources. This review focuses on a number of recent applications of these techniques to solve inorganic medicinal chemistry problems, focusing on studies of cellular uptake, distribution and biotransformation of established and potential therapeutic agents. The importance of using these synchrotron-based techniques to assist the development, or validate the chemistry behind, drug design is discussed.

Introduction

The cellular uptake, distribution and biotransformations associated with administration of a therapeutic agent are all crucial information for the medicinal chemist as they assist the design, understanding and development of a pharmaceutical. Importantly, the inorganic medicinal chemist can exploit the detection sensitivity and capabilities that synchrotron radiation techniques such as X-ray fluorescence (XRF) spectroscopy and X-ray absorption spectroscopy (XAS) possess for the detection and characterisation, respectively, of trace metals/metalloids associated with metallo-/metalloid- containing therapeutics in biological systems or fluids. While there are exceedingly sensitive analytical techniques available for this use such as high performance liquid chromatography (HPLC), graphite furnace atomic absorption spectrophotometry (GFAAS) and inductively-coupled plasma-mass spectrometry (ICP-MS),[1-2] these techniques fail to provide crucial spatial information regarding a drug in a tissue or cell. Also, in most cases the sample preparation (such as solvent extractions or acid digestion) associated with these techniques does not preserve important features/information such as the biological structure and/or the chemical speciation/structure of the drug or its metabolites.[1-2] As such, synchrotron radiation techniques such as microprobe XRF and XAS, offer unique advantages over laboratory-based techniques, as will be discussed in the following sections. While there are other microprobe techniques capable of relatively sensitive imaging, these are not the focus of this review and the reader is referred to the following references for information on these techniques.[3-5] In addition to XRF and XAS analysis of biological systems, synchrotron radiation-Fourier transform infrared (SR-FTIR) microspectroscopy has recently shown promise for rapid, high quality and high throughput analysis of biological samples, particularly cell samples. The latest applications of this technique for monitoring biomolecular changes associated with drug administration will be described.

Microprobe X-Ray Fluorescence Imaging

XRF spectroscopy is an analytical technique which involves the detection of emitted characteristic X-rays following excitation of the elements within the sample.[6-9] While electron, particle (protons or alpha particles), or X-ray beams can be employed as the exciting source for this analysis, the use of X-ray beams (from a synchrotron source) has been instrumental in the advancement of the technique in the area of microprobe XRF imaging for inorganic medicinal chemistry purposes.[5,8,10-11] Synchrotron radiation X-ray fluorescence (SRXRF) spectroscopy, also known as synchrotron radiation induced X-ray emission (SRIXE) spectroscopy, has become competitive with the earlier microprobe and nanoprobe techniques following the development of X-ray focusing devices, such as the Kirkpatrick-Baez (KB) mirror and the zone plate, that are capable of micron and submicron resolution, respectively.[12-15] There are two important features that contribute to the superb elemental sensitivities of microprobe SRXRF: (i) the absence of the continuum (*bremsstrahlung)* background radiation that is a feature of spectra obtained from charged particle beams, and (ii) the increased X-ray flux on the sample associated with the use of third generation synchrotron facilities.[5,16-18] Detection sensitivities have been reported in the ppb range, with values of 10^{-17}g - 10^{-14} g (depending on the particular element) cited for analysis of samples as small as individual mammalian (or even bacterial) cells.[6,16-22]

The physical process of XRF spectroscopy (**Figure 1**) involves the use of a beam that possesses an energy high enough to excite the atoms of all the elements of interest (*i.e.*, higher than the binding energy of the core electron of the element, generally K and L shells).[6-7] When the beam strikes the sample and a core electron is ejected into the continuum, an unstable ion is produced. An electron, from an outer energy level, drops down to fill the resultant vacancy and this is accompanied by the emission of an X-ray photon. The

energy of the X-ray photon is equal to the energy difference in the initial and final states of the transferred electron.[6-7] Since the electron transitions obey specific selection rules, the differences in energy levels are discrete and characteristic for a particular element, giving rise to characteristic X-rays that provide a unique identification for each element.[6,10,23] Binding energies and characteristic X-rays are documented for almost all elements ($Z \leq 95$) of the periodic table.[23] Most commonly, K and L lines are studied since the M and N line series are often masked by competing Auger interference.[6,8]

While XRF spectra can be collected at point locations within a sample, it is the mapping capabilities that are useful for studying the targeting action and metabolism of inorganic therapeutic agents within biological samples ranging from tumours to individual cancer cells.[3-4,24] The elemental imaging is performed by using a high precision XYZ motorized stage (up to 0.05 microns spatial resolution) that scans the sample in a rastor pattern in the path of the spatially fixed beam.[8,25-26] The sample is housed in a He or N_2 atmosphere to reduce the measurable component of Ar which is found in air. This is important for analysis of biological samples since the spectral position of the Ar K-shell fluorescence peak occurs in the region of P, S, Cl and K which are important endogenous elements.[8] Of the two gases, however, He is the preferred gas given that there will be close to no absorption of the emitted X-rays, whilst N_2 gas will absorb significantly (40% of 2 keV X-rays) in a 1-cm path.[27]

Microprobe XRF imaging of a metal-containing drug within a biological sample directly probes the metal based on the fundamental nature of the element. As such there is no need to tag or radiolabel the drug. [6,28] In the instance of detecting intracellular elements that are also endogenous, it is important that the introduced element is at significantly higher concentrations than in the control. Various sample forms can be studied depending on the required outcome.[8] Minimal sample preparation/interference is preferred when microprobe

SRXRF is combined with other techniques such as microprobe XAS or SRFTIR microspectroscopy, so that the integrity of the chemical structures within the sample are maintained. Samples such as cells or tissue can be grown or deposited on spectroscopically silent substrates, ideally silicon nitride membranes, formvar foils or polycarbonate foils [8,28-29]. Often rapid freezing/cryofixation and freeze-drying of tissue or cells are the protocols used for preparation of samples associated with XAS analysis.[8,15,19,28,30-34] Microprobe SRXRF analysis has also been performed on whole cells grown on silicon nitride membranes following fixation using glutaraldehyde or methanol.[35-36] For elements/drugs that possess reasonably strong interactions with intracellular biomolecules, thin-section analysis is beneficial as it facilitates high resolution imaging which is required for differentiation of organelles and provides confirmation of cell membrane penetration of the drug. The protocol for preparation of thin sections includes chemical fixation (*e.g.*, the use of glutaraldehyde in preference to formalin), dehydration, and resin infiltration. [8,28,32,34,37] The procedure is similar to that used for preparation of samples for transmission electron microscopy since it preserves the ultrastructure of the sample.[8,28,32,37] Details of these procedures are described in the referenced publications.[8,28,32,37] Unfortunately, no procedure for preparation of whole or thin-sectioned cells is free of uncertainty, which is why hydration and cryo-analysis, in the form of X-ray microtomography promises to be the desired micro-imaging technique in the future (see later Section).

Platinum-Containing Anti-Cancer Agents

Microprobe SRXRF imaging has been successfully used to probe the action of established and potential anti-cancer drugs.[26,38] One of the most studied class of drugs includes the platinum-containing drugs. This is unsurprising due to the therapeutic significance of cisplatin, carboplatin and oxaliplatin which are used in the treatment regimes of more than half of all cancer patients receiving chemotherapy.[38-39]

Since the Pt L_α peaks (Pt $L_{\alpha1}$ = 9.44 keV, Pt $L_{\alpha2}$ = 9.361 keV) coexist with that of the Zn K_β peak (Zn $K_{\beta1}$ = 9.572 keV), there are two approaches to the analysis of Pt in biological samples.[26,38] The first is the estimation of the Zn K_β contribution to the Pt L_α based on the known ratio of the Zn K_α peaks to the Zn K_β peak, followed by the subtraction of this value from the Pt L_α peaks.[26] The second approach is to perform the experiment at a higher energy (13.6 keV) that includes the Pt L_β peaks in the emitted X-rays and use these to estimate the Pt concentration.[38]

Microprobe SRXRF studies of cisplatin-treated A2780 ovarian carcinoma cells revealed predominant localisation of Pt in the nucleus with a small amount in the cytoplasm following 24 h exposure.[33] The uptake of Pt(II) and Pt(IV) potential anti-cancer agents by the A2780 cells with the metallointercalator, *cis*-[$PtCl_2$(2-[(3-aminopropyl)amino]-9,10-anthracene-dione)(NH_3)], revealed a high colocalisation of Pt and P maps which was attributed to Pt localisation in the cell nucleus.[38] A study of Br-labeled Pt(II) and Pt(IV)-treated cells was performed to probe the mechanisms of Pt anti-cancer activity. In the first instance, one of the amine ligands of cisplatin was substituted with a 3-bromopyridine ligand. Microprobe XRF analysis of the Pt(II)-treated cells showed colocalisation of Pt and Br in the nucleus.[38-39] The authors concluded that the coexistence of Br (as a brominated amine ligand) and Pt confirmed the strongly held belief that the amine ligands are non-leaving groups of Pt(II) complexes. In the second example, a Pt(IV) complex was prepared with a bromoacetate ligand in the axial position. A less intense Br map was obtained following treatment of the A2780 cells with the resultant Br-labelled Pt(IV) complex suggesting that reduction (and dissociation of the axial Br ligands) occurred prior to cell uptake.[38-39]

Microprobe SRXRF imaging has been reported for thin sections obtained from a tumour harvested from a mouse 3 h after injection with the Pt anti-cancer agent, *cis*, *trans*,

cis-[$PtCl_2(OH)_2(NH_3)_2$)].[38] The study revealed Pt and Zn co-localization in one area of a section of the tumour which the authors interpreted as corresponding to only one cell. The authors commented that identifying an appropriate sample area for imaging was an unexpected challenge.[38] Nonetheless, this could be an important area for future studies for confirming the potential clinical usefulness of metal-containing therapeutics.

Pt-Gd complexes have also been studied using microprobe SRXRF to determine the potential of these drugs for neutron capture therapy. Since ^{157}Gd possesses the largest effective nuclear cross-section, Gd(III) complexes are ideal agents for thermal neutron capture therapy employed for the destruction of tumour cells.[40] As a mechanism of achieving this, Rendina and coworkers[40] designed and synthesised the Pt-Gd complex that incorporated the DNA intercalating moiety, [Pt^{II}(terpy)] (terpy = 2,2':6'2''-terpyridine). Microprobe SRXRF of individual A549 human lung carcinoma cells treated with the Pt-Gd complex (5 μM) for 24 h showed the colocalisation of the Gd and Pt in the Zn and P regions of the cell which define the nucleus. Firstly, this result indicated that the Pt-Gd complex remained intact inside the cells. Secondly, the finding that Gd and Pt accumulated in the nucleus was extremely important since the effectiveness of Gd(III) neutron capture therapy relies on the ability of the complex to localise in close proximity to critical cellular components of the cancer cells.[40] In addition, statistical analysis of the intracellular K concentrations showed K increases of approximately 10× those of the control cells. The authors attributed this to: (i) a possible activation of Na^+/K^+ ATPase; (ii) the direct interaction of the drug with potassium ion channels that effectively trap K^+ in the cell; or (iii) the down regulation of potassium ion channel expression by targeting chromosomal DNA; although these hypotheses are yet to be confirmed.

In an extension of the aforementioned medicinal chemistry approach, Rendina and coworkers[41] studied the cellular uptake of the Pt(II)-carborane complex where the same Pt

containing moeity, [Pt^{II}(terpy)], was attached to carborane, the latter being important as a boron neutron capture therapeutic agent. In this instance, microprobe SRXRF was unable to show aggregation of Pt within the nucleus despite high levels of Pt found in the cells suggesting dissociation of the complex.[41]

Arsenic-Containing Anti-Cancer Drugs

Arsenic trioxide, marketed as Trisenox, was approved by the Food and Drug Administration in 2000 for the treatment of relapsed acute promyelocytic leukemia (APL).[42] Its clinical administration has been associated with a 65-80% complete remission rate.[42] This has prompted research into its mode(s) of action with the important goal of refining its administration and designing more efficacious As drugs for treatment of leukemias and solid tumours.[43-45]

SRXRF has been used for monitoring As along the length of the hair of APL patients receiving Trisenox treatment.[46] A beam (17 keV) of dimensions 10 × 3 μm^2 was used to scan 30-μm thick hair sections covering a length of 5 cm (corresponding to a period of 5 months hair growth).[46] The results demonstrated a rapid response of As content in the hair that reflected the different treatment regimes.[46] For instance, the As content in the hair showed expected fluctuations in a patient receiving non-continuous treatment over a period of 2 months.[46] In a more refined study led by the same author,[47] the X-ray beam (11.863 keV) was focussed to 1 × 3 μm^2 dimensions using a KB mirror and a sampling interval of 7 h was used. A steep increase in As content was observed within 24 h and reached more that half the maximum level.[47] The results were in agreement with the pharmacokinetics of rapid As absorption and elimination.[47] It was also observed that the As was distributed on the periphery of the cortex.[47] It was reported that this was similar to findings following external

As contamination of the hair which meant that one could not distinguish between ingested As or external As contamination based on its distribution through the cross-section of the hair.[47]

Microprobe SRXRF has also been used to probe the mechanisms of Trisenox therapy. HepG2 human hepatoma cells were imaged following administration of arsenite (the soluble form of Trisenox). Microprobe SRXRF showed that As accumulated in the euchromatin region of the cell nucleus following exposure to relatively high doses of arsenite (1 mM, 4 h, **Figure 2**).[32] This is consistent with As targeting DNA or proteins involved in DNA transcription. Subsequent studies of HL-60 cells (APL cells) that had been administered therapeutically relevant doses of arsenite (10 μM, 4 h) have also shown As localisation in the nucleus, and in some cases the nucleolus.[48] Intracellular concentrations were too low to confirm euchromatin localisation.[48] The additional ability of microprobe SRXRF to quantify intracellular elements was also highlighted in the article whereby differences in the relative distributions of Ca within the nucleus and cytoplasm were correlated with As treatment.[32] Increased nuclear Ca localisation was consistent with studies performed by Yee-Chien and Haimei[49] who showed that arsenite treatment of CHO-K1 cells also triggered Ca^{2+} accumulation. The ability of the technique to monitor intracellular Ca^{2+} is important since the loss of Ca^{2+} homeostatic control is an indicator of apoptosis. In addition, toxic agents that cause depletion in GSH (as is the case for arsenicals) can cause a concomitant influx of Ca^{2+} and perturb the intracellular Ca distribution.[50]

DNA Metallointercalator Agents

Microprobe SRXRF has been important for the medicinal chemist for establishing "proof of concept" with respect to the mode of action of particular drugs. A key example is the use of microprobe SRXRF for studying the uptake of metallointercalators to determine whether the complexes could target DNA, as intended in their design.[8] **Figure 3** shows the microprobe

SRXRF elemental maps of thin-sectioned cells obtained following the exposure of A549 lung cancer cells to cisplatin, or the metallointercalators, [56ME*SS*] ([5,6-dimethyl-1,10-phananthroline(1S,2D-diaminocyclohexane)platinum(III)]) or $[Ni(phen)(dppz)]^{2+}$ (phen = 1,10-phenanthroline, dppz = dipyrido[3,2-a:2',3'-c]phenazine) for 4 h. Thin-sections (1 μm) were mapped using a beam energy of 11.9 keV, focused to 0.2×0.15 μm^2 using two zone plates, and using a 0.3 μm step size (Beamline 2-ID-D, Advanced Photon Source, Argonne National Laboratories). The results were promising, since the microprobe SRXRF studies were the first to show that both Pt and Ni clearly localised in the cell nucleus following treatment with [56ME*SS*] or $[Ni(phen)(dppz)]^{2+}$, respectively. Furthermore, it was clear that the localisation occurred in the heterochromatin region of the nucleus; *i.e.*, in the vicinity of the densely packed DNA.[8]

Metallocene Anti-Cancer Agents

Microprobe SRXRF imaging of metallocene-treated V79 Chinese hamster lung cells was also performed since it has been reported (over 30 years ago) that metallocene dihalide complexes exhibit anti-tumour activity.[31,51] Complexes of the structure, Cp_2MCl_2 where Cp = η^5-cyclopentadienyl and M = Mo, Nb, Ti or V were studied to differentiate between the cellular targeting properties of the specific metal complexes since DNA (specifically nucleic acid rich regions of solid Erhlich ascites tumour cells) had been implicated as the primary target for Cp_2TiCl_2 and Cp_2VCl_2, with Cp_2TiCl_2 undergoing phase I and II clinical trials. In contrast, no data existed for the Mo and Nb complexes and it was important to evaluate whether these complexes also possessed promising properties that warranted preclinical studies.[31] Unfortunately, microprobe SRXRF analysis of whole cells that had been treated with IC_{50} concentrations of Cp_2TiCl_2 or Cp_2VCl_2 (100 μM and 10 μM, respectively, for 24 h) showed

only small increases in the Ti and V concentrations that were not considered significantly higher than the control cells using the Dunnett test.[31] It was concluded that the intracellular concentrations must have been at the detection limit of the technique. In contrast, significant increases in the intracellular Mo concentrations were obtained following treatment of the V79 cells with Cp_2MoCl_2 (800 μM, 24 h) or $Cp_2Mo(SC_6F_4COONa)_2$ (800 μM, 24 h).[31] Similarly, increased cellular Nb was detected in cells treated with Cp_2NbCl_2 (250 μM, 24 h). One of the greatest challenges of the study was the simultaneous detection of Mo and the important endogenous elements, given that the use of the 20.5 keV beam for detection of Mo resulted in poorer detection of the lower energy elements such as K, Cl, S, and P.[31] In efforts to overcome this, dual mapping was performed at 10 keV and 20.5 keV using coordinates generated from alphabetised Finder grids.[31] The resultant images showed colocalisation of Mo with K and Zn indicating the ability of Cp_2MoCl_2 to traverse the nuclear membrane and accumulate in the nucleus.[31]

Nanoparticles and Nanoconjugates

A rapidly emerging area of medicinal chemistry is the use of nanoparticles as direct therapeutic agents, drug delivery agents, and even diagnostic agents.[35,52-53] Consequently, it is not surprising that microprobe SRXRF is becoming recognised as a technique for imaging intracellular nanoparticles in efforts to develop and confirm the capabilities of these agents.[35,52] An exciting study has been reported by Paunesku *et al.*[52] whereby they aimed to produce DNA-targeting TiO_2 nanoparticles that could be excited, causing the electropositive holes of the semiconductor to be injected into the DNA, ultimately leading to DNA scission. The important role of microprobe SRXRF was to establish whether these nanoparticles could be taken up by the cells and retained at their target DNA sequence.[52] Two DNA targets were studied, those of ribosomal RNA located in the nucleoli or the mitochondria. It was shown that the different nanoconjugates were retained in detectable

quantities exclusively in the subcellular compartments that they were designed to target.[52] The authors also used microprobe SRXRF to show that inclusion of the contrast agent, Gd(III), into the nanoparticle to produce Gd(III)-modified DNA-TiO_2 nanoconjugates, also resulted in a structure capable of specific organelle targeting.[54] The interest in this result was that the complex possessed the added ability of being detectable by magnetic resonance.[54]

Hard X-Ray Fluorescence Tomography.

Plane-polarized XRF was proposed more than a decade ago for whole body imaging in order to take advantage of the fact that XRF is a non-invasive technique, capable of highly sensitive elemental analysis.[55] A typical and highly desirable application of the technique was to image the platinum concentration associated with administration of the drug, cisplatin (or its transplatin analogues).[55] The goal was to provide clinical information regarding its *in vivo* distribution and in so doing, assist in establishing dose-response relationships, for optimising and maximising therapeutic effect and minimising toxicity and cost.[55] The minimum detectable concentration (MDC) increased with increasing depth of the tumour due to the attenuation effect. Also the estimated MDC's ranged from 5.6-38.1 ppm depending on the tumour depth (reported as 20-35 mm, respectively) and radiation dose applied.[55] A number of challenges need to be overcome, however, before this becomes a more widely used technique.

Microprobe XRF tomography has also been proposed as an exciting technique capable of 3-D imaging of trace elements in biological tissues and cells whereby sub-500 nm resolution XRF tomography is now possible. To date, SRXRF microtomography of bound Pt in DLD-1 human colon carcinoma spheroids has successfully monitored the depth of

penetration of cisplatin and three Pt(IV) complexes after 24 h exposure.[56] The technique detected 10 ppm Pt in the cancer spheroids and showed enrichment of the Pt in the outer region (corresponding to the outer proliferative region) and uniform distribution deeper within the spheroid.[56] In addition, the study showed poorer but similar penetration profiles of Pt(IV) complexes in comparison to cisplatin and represents an interesting future mechanism for studying the efficiency of other anti-cancer agents.[56]

While not a medicinal chemistry application, de Jonge and Vogt[57] have performed higher resolution imaging of the whole diatom, *Cyclotella meneghiniana,* with 150-nm voxels over a 15-µm field of view. An exciting prospect of the technique would be the incorporation of cryocapabilities which would enable the 3-D elemental analysis of frozen-hydrated specimens. Biological tissues and cells analysed by this technique would require minimal sample preparation, reducing concerns regarding the difficulties and artefacts associated with sample preparation and serial thin-sectioning.[57] Despite the exciting promise of this technique, however, SRXRF microtomography has not yet found general application. This is due to technical challenges combined with the required data acquisition times, for *e.g.* de Jonge and Vogt[57] calculated that analysis of a 10 μm^3 specimen, performed at 30 nm resolution and 300 projections, would take 8 h. The consequential use of a smaller sample size decreases the statistical power of the analysis and raises the question of the reliability of any conclusions. Another challenge of SRXRF tomography, as alluded to in the case of whole body analysis, is self-absorption.[55,57] Existing corrections of self absorption assume that the X-rays are confined to and are absorbed only by the voxels within the imaged specimen plane, which is unrealistic.[57] As such further progress needs to occur before this technique can become routine and impact on medicinal chemistry research in the clinic. Fortunately, self-absorption will be less significant with smaller samples, such as individual cells.

X-Ray Absorption Spectroscopy

XAS is an important tool for studying most elements of the periodic table and it has been extremely useful for studying transition metals and metalloids. It is specifically useful for studying metals that are otherwise spectroscopically silent; *i.e.*, those that possess filled or empty d-shells and have no spectroscopic signature.[58] XAS is beneficial for the study of bioinorganic systems such as metal- and metalloid-containing drugs and enzymes since it is an extremely versatile and highly sensitive technique capable of providing information regarding metals in many physical states and chemical environments.[58-60] The technique can be applied to bulk or microprobe analyses of samples which include: solids, biological solutions, electrophoresis gels, and healthy or diseased mammalian cells and tissue.[58-60]

XAS, in contrast to XRF spectroscopy, cannot feasibly be performed using a laboratory X-ray source. Instead the highly intense and tunable X-rays generated at a synchrotron are essential for XAS.[61] The instrumental setup for XAS is shown in **Figure 4** where it is apparent that XAS data can be collected in two modes: fluorescence mode or transmission mode. Normally the technique is performed in transmission mode; however, in the case of trace elemental speciation such as those associated with biological samples, (*i.e.* those of dilute concentrations associated with proteins, bulk or single cells) the technique is often performed in fluorescence mode since it imparts greater sensitivity.[61]

The principles for XAS are outlined briefly; however, the reader is referred to reviews for a more detailed description.[58,62-65] An X-ray absorption spectrum is generated by subjecting the sample to a tuneable X-ray beam produced by a synchrotron source. The X-ray beam energy is swept across an energy range that encompasses the binding energy of the element of interest. When the X-rays have sufficient energy to eject a core electron to an

orbital (that is partially filled or empty) or to the continuum, there is an abrupt increase in the absorption coefficient, which gives rise to the dominant feature of the XAS spectrum (**Figure 5**) known as the "absorption edge".[58] The XAS spectrum can be divided into two main regions: the X-ray absorption near edge structure (XANES) and extended X-ray absorption fine structure (EXAFS) regions, which contain extremely useful information regarding the local structural environment of the element of interest.[58]

The XANES spectrum is typically defined as the region immediately within approximately 50 eV of the edge. Key features of the XANES spectrum include the aforementioned edge, and the white line peak which occurs directly after the edge. The XANES spectrum is sensitive to the oxidation state, the immediate coordinating atoms, and the electronic structure of the absorber atom.[58,62-63] It provides information regarding the average coordination environment of the absorber atom and can be used to provide qualitative information.[58,62-63] Typically, increases in the oxidation state are associated with increases in the energy associated with the absorption edge, since greater energy is required to eject the core electron.[58,62-63] Caution must be used when relying on the spectral edge position to interpret the oxidation state, however, since the coordinating atoms also influence the edge energy. For instance, while the oxidation state does not change, a slight decrease on the local charge of the absorber element brought about by coordination to a less electron-withdrawing atom (*e.g.* S versus O) would result in a lower edge energy.[58] In addition, and complementary to this, the edge energy can be influenced by the metal-ligand bond distance, with the edge energy expected to vary inversely with the square of the metal-ligand distance.[58] Another factor that is observed in the XANES spectrum is that the features become broadened when the coordination environment becomes less symmetric, giving rise to a less intense white line.[58] A typical example of this is the more symmetrical crystalline small-molecule models compared with their protein- or peptide- bound analogues.[58] In

some cases a pre-edge peak is also observed. Weak pre-edge peaks for the K edge first row transition metals are observed for the forbidden (dipole selection rules) 1s $\rightarrow$ 3d transition. They occur for metals that have an unfilled 3d shell and provide an indicator of coordination geometry. For instance, the centrosymmetric octahedral Cr(III) complex exhibits the weakest pre-edge feature, while the loss of centrosymmetry associated with trigonal bipyramidal and tetrahedral complexes is associated with an increase in the intensity of the pre-edge peak.[66-69] This phenomenon is due to the mixing of the 3d and 4p orbitals and direct quadrupolar coupling.[58,66]

The EXAFS spectrum extends to higher energies and contains more subtle features (**Figure 5**). It results from the interaction of the ejected electron with the surrounding atoms and is distinguished by a wavelike structure indicative of the constructive and destructive interference from which it is generated. For more detailed information regarding the principles of EXAFS the reader is referred to the cited reviews.[8,58,64-65]

Both XANES and EXAFS have played essential roles in the analysis of proteins and enzymes in cells. Micro-XANES/EXAFS utilises focusing devices (KB mirrors or zone plates) that focus the beam to micron or submicron dimensions, enabling analysis of cellular and subcellular structures. To date micro-XANES analysis has provided information regarding metals associated with diseased states, such as Fe(II/III) located in the neuronal cells of subjects exhibiting Alzheimers and Parkinsons diseases,[70] Cu(I)/Cu(II) in dopeminergic cells associated with Parkinson's disease, and Zn concentrations associated with prostate cancer.[70] The focus of the following sections, however, is on the use of XANES and EXAFS (and the microprobe applications of these) to study the chemical structure of therapeutic agents prior to and after cell uptake in order to probe their biotransformations within cells.

Platinum-Containing Anti-Cancer Agents

Both XANES and EXAFS have been used by medicinal chemists to characterise metal-containing drugs in solution, formulations, and biological media. Some of the most prominent studies include those associated with the anti-cancer drug, cisplatin. Solutions of the platinum-containing drug, cisplatin,[71] and its derivative, oxaliplatin,[72] have been analysed by bulk XAS to confirm the presence of axial water ligands. Bulk XAS has also been used for the development of controlled release drug delivery systems by confirming the integrity of drugs in the delivery agent; a specific example being the use of XAS to confirm that the structure of cisplatin did not alter following its incorporation into poly(ethylene oxide) gel.[73]

Hambley and coworkers[33,74-75] used bulk XAS to determine the ability of Pt-treated cancer cells to reduce Pt(IV) complexes to the potentially more active Pt(II) anti-cancer agents. Predictably, the position of the edge assisted in the differentiation (2.2 eV difference) of Pt(II) from Pt(IV).[33,74] So too did the ratio of the intensity of the white line peak to the post-edge region.[33,74] In recent efforts to try to combat cisplatin resistance, Hambley and coworkers[75] prepared monomeric Pt(IV) analogues, [*trans,mer*-[$PtCl(OH)_2$] and [trans,mer-[PtCl(dien)], of the potent polynuclear platinum complex, [trans-$PtCl(NH_3)_2)_2${μ-trans-$Pt(NH_3)_2(NH_2(CH_2)_6NH_2)_2$}]$^{4+}$, since the latter complex had been withdrawn from phase II clinical trials due to side effects (despite earlier promise).[75] Human ovarian A2780 carcinoma cells were treated with the Pt(IV) drug and analysis of the XANES spectra with respect to the standard curve, prepared from the ratio of the peak height to the post-edge intensity for known ratios of Pt(II) to Pt(IV), was performed. It was found that 38% of the drug had reduced to Pt(II) in the first 2 h while most of the drug (87%) had converted to Pt(II) within 24 h. They concluded that the improved intracellular stability of the triammine

complex highlights the importance of preparation and testing of the Pt(IV) polynuclear complex.[75]

Arsenic-Containing Anti-Cancer Agents

In a pharmaceutical-directed study, Nicolis *et al.*[76], used XAS to characterise arsenic in the injectible arsenic trioxide formulations used to treat APL patients. Unsurprisingly, XANES spectroscopy showed that the As species was As(III) while EXAFS analysis indicated that the arsenic was coordinated to three oxygen atoms at a distance of 1.779 Å, similar to arsenous acid.[76] Nicolis, *et al.*[47] also performed XANES studies of As in the hair of APL sufferers following Trisenox administration. They reported that the As was not S-bound but was O- or N- bound. They attributed this finding to the fact that the cysteine residues of keratin are engaged in cystine sulphur bridges.[47]

Multiple linear regression analysis of XANES spectra and EXAFS analysis of spectra obtained from arsenite-treated HepG2 human hepatoma cells (100 μM, 4 h) were employed to shed light on the As metabolites formed following high dose exposure. The predominance of As tris-sulfur species provided increased credence to the likelihood that the dominant interactions of As occurred with nuclear proteins and potentially act as a key factor in As-induced cancer toxicity.[32]

Bacquart *et al.*[77] performed microprobe XANES of As located (by microprobe SRXRF) in the nucleus, cytosol and mitochondrial network of arsenic trioxide-treated human ovarian adenocarcinoma (IGROV1) cells. The instrumental set-up involved the use of a liquid nitrogen cryo-stream to reduce radiation damage to the sample. It was found that the predominant species in the IGROV1 cells, and that responsible for toxicity, was $As(OH)_3$ since metabolism was negligible in the cell line.[77] In contrast, microprobe-XANES analysis of HepG2 cells treated with $As(OH)_3$ showed small edge energy shifts of the As XANES

spectra that were dependent on the organelles (average edge energies: arsenic trioxide, 11871.5 eV; nucleus, 11870.7 eV; cytosol and mitochondrial network, 11871.2 eV) indicating differences in As speciation.[77] Exposure to low concentrations of arsenite (10 μM, for 24 h vs 100 μM, 4h in the study described above)[32,77] also resulted in predominance of As(III), although there was some evidence of mixed valence As (As(III)/As(V)) in the nucleus of one of the nine cells analysed.[77]

Other Anti-Cancer Agents

XANES analysis of intracellular cobalt has been important for the development of cobalt complexes as potential hypoxia-activated prodrugs.[78-80] The concept was to exploit the hypoxic nature of tumours whereby the inert Co(III) complexes could be reduced to the labile Co(II) complexes in the reducing environment, and subsequently release an active anti-cancer agent.[78-80] The XANES studies involved the systematic study of a mixture of Co(III) and Co(II) complexes to differentiate between the oxidation states.[78] It was noted that the analysis of Co in cells was complicated by changes in the coordination sphere of Co(III) complexes, and that XANES was useful for monitoring the oxidation state as long as the ligand exchange reactions of Co(III) were slow relative to the reduction to Co(II).[78] While the XANES of intracellular Co obtained from [Co(diNOsar]Br_3-treated cells reflected that of the solution spectra of the complex, it was found that the spectra obtained from [$Co(acac)_3$]- and [Na[$Co(acac)_3$]-treated cells reflected a mixture of intracellular products. indicating a loss of the carrier ligands .[80]

EXAFS in conjunction with the new synchrotron based technique, nuclear resonance vibrational spectroscopy (NRVS), and density functional theory calculations was used to probe the anti-cancer mechanisms of the glycopeptide, bleomycin.[81] Bleomycin is an effective chemotherapeutic agent used to treat Hodgkins lymphoma and head, neck, and

testicular cancers. It is believed to complex to Fe *in vivo* to facilitate DNA double strand scission via a reaction of Fe^{III}BLM with O_2 and an electron, or through a shunt reaction between Fe^{II}BLM and H_2O_2.[81] Following the study, it was concluded that the active species were (BLM)Fe^{III}-OH and (BLM)$Fe^{III}(\eta^1$-OOH) and that direct H-atom abstraction is the thermodynamically favoured pathway over other proposed pathways.[81]

Anti-Malarial Drugs

EXAFS of Fe has also been conducted to improve the understanding of the mechanism of action of the anti-malarial drug, chloroquine.[82] It is known that malaria parasites are susceptible to quinoline based drugs only at the time of hemoglobin degradation and production of malarial pigment.[82] The parasite digests the peptide chains of the host's hemoglobin and needs to dispose of the remaining heme to avoid toxicity and death of the parasite. It is believed that quinoline drugs complex to the resultant heme and prevent their disposal. Walczak *et al* [82] claimed that, it was impractical to directly study infected blood samples from patients treated with chloroquine, given the fact that there is Fe associated with hemoglobin as well as the heme remaining from the parasites' digestion. Consequently, they performed XAS of the synthetic substitute, mesohematin anhydride, in acidic solvent (to simulate the parasite's food vacuole) in the presence of the drug. [82] They observed differences between the synthetic equivalent of hemozoin in the powder state compared to the aqueous state (in acetic acid and water) at different concentrations that mimicked the physiological condition of the parasite's food vacuole. Additional changes were also observed following the addition of the anti-malarial drug, chloroquine.[82]

Anti-Inflammatory Agents

One of the earliest medicinal chemistry uses of XAS was the study of the biotransformation products of gold-based rheumatoid arthritis drugs.[83] Aurosomes isolated from Sprague-

Dawley rats that had been injected (intraperitoneally) with sodium gold(I)thiomalate (0.4 mg Au/kg, weekly for 20 weeks) or gold(III) tetrachloride (35 mg Au/kg, single dose) were analysed using XANES.[83] XANES spectra revealed that the gold associated with the aurosomes following treatment with sodium gold(I)thiomalate was Au(I).[83] In addition, Au(I) was also identified in the aurosomes of rats that had been treated with gold(III) tetrachloride indicating the *in vivo* reduction of Au(III).[83] EXAFS analysis revealed that the Au resulting from administration of gold(I)thiomalate was coordinated to two sulfur atoms which were believed to be of cysteine (protein) or glutathione origin.[83] While reported in the context of Au anti-proliferative agents, Messori *et al.* recently performed XAS studies of the interactions of auranofin with the human plasma proteins, bovine serum albumin and serum apotransferrin.[84] The Au(I) oxidation state was conserved during protein binding and the mechanism was believed to occur through release of the thiosugar ligand to facilitate replacement with a thiol or thioether from the protein.[84]

The use of XAS for the development of copper containing NSAIDs, such as $[Cu_2(indo)_4L_2]$, indo = (1-(4-chlorobenzoyl)-5-methoxy-2-methyl-1H-indole-3-acetate) and L = solvent ligands, played a crucial role in the development of veterinary and human nonsteroidal anti-inflammatory formulations, the latter proceeding to human clinical trials.[85] XAS was used to explore the chemical and physical properties of the formulations with emphasis on modelling the dimeric $Cu_2O_{10}C_8$ core in the dimeric Cu(II) complex and examining any changes in it as a result of changes in the axial ligands.[85] The flexibility of the technique for analysing injectable formulations, gels, ointments, and pastes highlights its usefulness for characterising pharmaceuticals for registration. Similarly, EXAFS was also applied for the successful characterisation of mononuclear and dinuclear zinc-indomethacin complexes.[86]

Ruthenium Anti-Metastatic Agents

Emerging drugs (in phase I clinical trials) such as the potential Ru(III) chorido-indazole anti cancer drug (KP1019) and the anti-metastatic agent, NAMI-A,[87-88] have been analysed in cell culture media, blood serum and cultured mammalian cells to understand the transformations that occur to the metal centre. Lay and coworkers[89] isolated Ru(III)-BSA complexes by gel-filtration chromatography, freeze-dried the product and analysed it by XAS.[89] The resultant spectra were compared with the parent Ru(III) complex, and model Ru(III) complexes containing predominantly Cl^-, NH_3, or CH_3COO^- ligands.[89] Linear regression analysis of the post-edge regions of the XANES spectra revealed that the Ru(III)-BSA spectrum was best characterised by a model consisting of 65% Ru bound to N, and 35% Ru bound to O, suggesting replacement of the original Cl^- ligands with protein N-donors and carboxylato residues.[89] The authors concluded that the XAS evidence, suggesting that >90% of the Ru(III) complex binds to blood albumin, is consistent with its low toxicity but high anti-metastatic efficacy.[89]

Dietary Supplements

Multiple linear regression analyses of XANES spectra have been used for characterisation of Cr(III) anti-diabetic supplements including $[Cr_3O(OCOEt)_6(OH_2)_3]^+$, $[Cr(pic)_3]$ (pic = 2-pyridinecarboxylato) and *trans*-$[CrCl_2(OH_2)_4]^+$ (introduced as $CrCl_3.6H_2O$) in biological fluids and in cultured cells.[90] It was found that $[Cr_3O(OCOEt)_6(OH_2)_3]^+$ and $[Cr(pic)_3]$ underwent extensive ligand exchange reactions in solutions that simulated gastric and intestinal conditions and in the presence of blood serum and cell culture medium.[90] The resultant products were identified as Cr(III) complexes coordinated to hydroxo and amino acid ligands.[90] Concern was raised over the finding that reactions of $[Cr(pic)_3]$ with serum enhanced its propensity to be converted to carcinogenic Cr(VI) by biological oxidants.[90]

The speciation of common selenoamino acid supplements, selenomethionine (SeMet) and Se-methylselenocysteine (MeSeCys) in A549 human lung cancer cells has also been investigated using XAS.[91] The value of this research stems from the fact that the essential element, Se, has been linked to reductions in the cancer incidence and mortality when administered at supranutritional doses.[91] MeSeCys is believed to be the more effective chemopreventative agent of the two complexes since MeSeCys is known to produce MeSeH more efficiently than SeMet.[91] Linear combination fitting of the XAS spectra of the Se standards to those obtained from the cell pellets treated (24 h) with the supplements showed that Se was found exclusively in the carbon bound form in SeMet-treated cells while a diselenide component was also identified in MeSeCys-treated cells, indicating that there was a difference in the metabolism of the supplements.[91] It was suggested that the presence of the diselenide component in the MeSeCys-treated cells may be due to the cleavage of MeSeCys by β-lyase to produce the active anti-carcinogenic compound, MeSeH.[91]

Synchrotron Radiation – Fourier Transform Infrared Microspectroscopy

The application of vibrational spectroscopy for the detection of disease in human tissue and cells commenced in the early 1990's and escalated following the development of lab-based and later, synchrotron radiation-based infrared microspectroscopy.[92] There have since been significant developments towards disease diagnosis, improvements in the understanding of disease progression and validations of hypotheses regarding diseases such as prostate,[93] skin,[94] colon,[95] cervical,[94,96] and breast cancers,[97] melanoma,[98] leukemia,[99] transmissible spongiform encephalopathies/prion diseases,[100] Alzheimers disease,[101-102] diabetes,[103] malaria,[104] ophthalmic disorders,[105] and arthritic disorders.[94,99]

The usefulness of SR-FTIR microspectroscopy derives from the fact that the IR source is 10-1000 times more brilliant than the conventional globar source.[106-107] This equates to superior signal to noise ratios in the resultant spectra, improving acquisition times and spatial resolution, both of which are important for analysing biological samples.[92,106] As such, recent attention has been focussed on the use of SR-FTIR microspectroscopy for the study of biomolecular changes that occur following the administration of drugs or potential therapeutic agents in diseased cells.[92,108-112] Importantly, macromolecules associated with biological samples produce signature IR bands that can be readily discerned from the IR spectra.[94,99,113-114] Typical spectral features include: amide I (ν ~1650 cm^{-1}) and amide II (ν ~1549 cm^{-1}) bands representative of proteins; symmetric (~1080 cm^{-1}) and anti-symmetric PO_2^- (~1232 cm^{-1}) bands associated with DNA; C-H stretches of $-CH_3$ (ν_{as} ~2955 cm^{-1}) and $-CH_2$ (ν_{as} ~2850 cm^{-1}), the ester band (1740 cm^{-1}) and the C-O-P (~1080 cm^{-1}) band associated with lipids/phospholipids; and C-O stretches (1050 cm^{-1}) of carbohydrates.[94,99,113-114] In addition, changes in the average protein secondary structure can be detected by analysing the components of the amide I band. For instance, specific secondary structural assignments include: α-helices (1645-1662 cm^{-1}), β-sheets (1613-1637 cm^{-1}), turns (1662-1682 cm^{-1}) and random coils (1637-1645 cm^{-1}).[99,113,115-117]

A recently emerging medicinal chemistry application of SR-FTIR microspectroscopy is the analysis of fixed and live cancer cells to detect biomolecular changes that occur following drug treatment. The interest in the use of this technique stems from an urgent demand for the development of accurate and cost-saving analytical techniques that can be applied to the screening of new drug candidates.[109] The analysis involves the collection of spectra from large numbers of cells (generally >100 cells per sample) following exposure to the therapeutic agent, and the objective analysis of the resultant data through statistical

procedures such as principal component analysis (PCA) and hierarchical cluster analysis.[92] While changes in spectral features can often be visually observed in average spectra, tools such as PCA remove subjectivity and add credence to the evaluation of any biomolecular differences/similarities in the spectra of cell or tissue samples.[118] SR-FTIR can be used for mapping individual cells and tissues;[119-120] however, this is diffraction limited and noise becomes apparent at approximately 1000 cm^{-1} when an aperture of 5 μm^2 or smaller is used.[106] Currently, there a a number of new promising developments in progress to try and overcome this limitation as described within the cited review.[24]

One of the most important challenges of SR-FTIR analysis of single cells is overcoming issues of highly distorted baselines, and derivative-like peak shapes, which are associated with small (<10 μm) cells and specifically affect strong bands such as the amide I band.[92,107] In an effort to try to separate biochemical-induced effects from those of the physical shape and size of the cells that lead to the IR baseline abnormalities, Gardner and coworkers have developed correction algorithms that reduce the distortions caused by resonant Mie scattering.[92,107,121] These have been implemented in a number of studies.[92,122-124]

Anti-Cancer Agents

A typical example of the use of SR-FTIR microspectroscopy for monitoring therapeutic effects was the study of the spectral changes on non-small cell lung cancer cells (Calu-1) following administration with cytostatic doses (0.1-100 nM) of the anti-tumour drug, gemcitabine, for 24-72 h.[108] The study showed complimentarity between spectra obtained from individual cells using SR-FTIR versus those obtained from bulk cell populations using a conventional laboratory IR.[108] Hierarchical cluster analysis of spectral windows showed dose- and time-dependent effects of the drug. Draux *et al.*[108] reported increases in the molecular vibrations corresponding to characteristic bands of proteins and RNA and it was

concluded that these IR changes may be related to the molecular mechanism of the cytostatic drug and the accumulation of the cells in G1 phase.[108]

Bellisola, *et al.*[109] performed SR-FTIR microspectroscopy of chronic myeloid leukaemia (K562) cells to identify signatures of apoptosis following administration of a drug that directly targets the BCR/ABL oncogene protein, imatinib mesylate (4-[(4-methylpiperazin-1-yl)methyl)-*N*-[4-methyl-3-[(4-pyridin-3-ylpyrimidin-2yl)amino]-phenyl]benzamide), and a drug that indirectly targets the BCR/ABO oncogene protein, FTY720 (2-amino-2-[2-(4-octylphenyl)ethyl]-1,3-propanediol hydrochloride). The authors performed complimentary techniques such as Western Blotting analysis and were able to identify and cross-validate some IR signatures induced by the imatinib mesylate in the K562 cells.[109] For instance, they concluded that significant changes that occurred in the interval 1290-900 cm^{-1} and in particular between 940-900 cm^{-1}, were associated with changes in the PO stretching mode in the phosphorylated proteins.[109] This was significant because the drug was known to cause a rapid decrease of protein tyrosine phosphorylation.[109]

Mantsch and coworkers[125] have also used SR-FTIR microspectroscopy for the detection of apoptosis in K562 cells and the T-lymphoblastic cell line (CEM cells), with the aim of determining its feasibility as an indicator of chemosensitivity of leukaemia cells isolated from individual patients. They noted greater changes in the CEM cells (52.8%) versus K562 cells (15.67%) after 24 h exposure to the drug, etoposide, and found excellent correlation with the percentage of apoptosis observed by flow cytometry results.[125] It was also concluded that SR-FTIR microspectroscopy was able to detect apoptosis after 4 h compared to 6 h using flow cytometry.[125]

SR-FTIR microspectroscopy was performed on A2780 ovarian cells that had been treated with a new di-gold(I) organometallic complex, [1,3-$(Ph_3PAu)_2C_6H_4$], that was found

to exhibit cytotoxic activity *in vitro*.[92] The interest in the drug stemmed from the fact that it induced little to no resistance against cisplatin resistant cells which implied that the drug acted by different mechanism(s).[92] Following the application of Mie scatter correction, there was significant differentiation between the cell spectra obtained on treatment with different drugs which fitted with different *in vitro* cell culture behaviour.[92] PC2 differences were observed following the comparison of the control versus cisplatin or cisplatin versus [1,3-$(Ph_3PAu)_2$-C_6H_4]-treated cells.[92]

Photodynamic Therapeutic Agents

Another example where SR-FTIR has been used for the evaluation of therapeutic effects includes the area of photodynamic therapy (PDT).[111] PDT is based on the interaction of light with a photosensitiser which, in turn, results in the production of radical species that induce the death of cells in close proximity. For instance, PDT has potential for treatment of cancerous cells (*e.g.*, skin cancers) and infectious organisms.[111] Chio-Srichan *et al.*[111] studied the effect of Hypocrellin A in HeLa cells as a function of incubation time since it reportedly possessed anti-cancer activity when irradiated with light. PCA of the SR-FTIR spectra obtained from cells administered Hypocrellin A followed by irradiation (10 J cm^{-2} dose at 460 nm) revealed changes in the protein secondary structures, whereby a shift of the amide I band from 1650 cm^{-1} to 1630 cm^{-1} was attributed to a contribution of increased secondary β-sheet structure.[111] Decreases in the peaks in the region 1000-1300 cm^{-1}, associated with DNA, were also observed.[111] This was attributed to a higher optical density of condensed DNA, consistent with transmission electron microscopic evidence.[111]

The PDT potential of 4,5-benzoindotricarbocyanine (indocyanine green, ICG) as a treatment for human melanoma was also assessed by SR-FTIR microspectroscopy.[112] Previously, the poor success of PDT with melanomas was believed to stem from their high

content of melanin which acts as a screen for white light. Consequently, ICG was proposed since it absorbs light in the range 700-800 nm, where melanins do not absorb. SR-FTIR analysis was performed on human skin melanoma cells (Sk-Mel-28) treated with ICG followed by PDT.[112] Cluster analysis of the resultant IR spectra revealed a decrease in the nucleic acid phosphate absorption modes at 1240 and 1180 cm^{-1} in the ICG/PDT-treated cells which was consistent with DNA fragmentation of the apoptotic cells.[112] Additionally, there were protein conformational changes associated with protein denaturation and increases in the lipid bands suggesting redistribution of the phospholipids within the cell membrane (*i.e.*, externalisation of phosphatidyl serine).[112]

Live Cell SR-FTIR Microscopic Analysis

Although an experimental challenge, live cell analysis under aqueous media is desirable as it removes the potential for spectral artifacts resulting from fixation procedures and provides the added advantage of allowing real time analyses.[110,126-128] SR-FTIR microspectroscopy was used to analyze live leukemia cells following their exposure to Trisenox™, administered in the form of sodium arsenite (100 μM).[110] The procedure involved the use of a demountable liquid cell comprising a 1-mm thick CaF_2 window onto which a spacer had been patterned by polymer spin coating and UV photolithography, and an upper 0.5-mm thick CaF_2 window **(Figure 6A)**.[110,126] The two windows were held tightly together in a Thermo micro compression cell **(Figure 6B)** in order to reduce the aqueous sample volume. The design of the sample holder enabled the collection of high quality spectra from a solution that was less than 20 μL. This meant that the spectra were not dominated by OH deformation **(Figure 6D).**[110,126] Exposure of the HL-60 cells to the anti-leukemia drug resulted in significant spectral differences within 40 min exposure. The most prominent differences (as determined by the second derivative spectra and PCA) occurred in the protein region of the

spectrum, where the dominant contribution to the amide I band shifted from 1639 cm^{-1} (β-sheet) in the control cells to 1650 cm^{-1} (α-helix) in the arsenite-treated cells.[110] The overall results of this study indicated that the mechanisms of action of arsenite-induced toxicity involved alterations to the protein structure and interactions with DNA.[110]

One of the drawbacks of the demountable liquid cell described above was the slow loss of the media, over the period of 2 h, limiting long term exposures and data collection.[110,126] Subsequent improvements to the design have been made whereby the lithography fabricated spacer has been changed from a single outlet channel to three zig-zag channels **(Figure 6C),** which effectively slow down the loss of the solution.[126] An alternative live cell sample holder was reported by Holman *et al.*,[128] which was a custom made on-stage mini incubator. It allowed *in situ* SR-FTIR collection of spectra from cells while maintaining a proper moisture and growth environment.[128] Clearly, the success of such devices, which enable long term monitoring of the sample, will provide invaluable insights into the mechanisms and kinetics of drug-induced cell modifications.

Combination of SR-FTIR and Fluorescence Microscopy for Simultaneous Analysis

The combination of SR-FTIR microscopy with fluorescence microscopy at the same beamline was documented in 2002.[102] For the first time, an IR microscope had been modified to allow simultaneous fluorescence sample visualisation and IR analysis.[102] The capabilities were exploited for experiments ranging from studies of osteoporosis, to Alzheimer's diseased brain tissue, to cell apoptosis.[102] The most sophisticated of the experiments was the study of the effect of the drug, nandrolone decanoate (an anabolic steroid that enhances bone density in osteoporotic women) in female monkeys that had undergone ovariectomies to induce osteoporosis.[102,129] The monkeys were administered different fluorochrome labels at 1 (calcein) and 2 years (alizarin) after the ovariectomy, to

identify the new bone using fluorescence microscope. The areas were analysed by SR-FTIR microspectroscopy and the phosphate/protein ratio was studied with reference to control monkeys. The results showed a reduced rate of bone mineralisation in ovariectomised monkeys versus the control. Furthermore, the mineralisation was also effected in the monkeys treated with nandrolone decanoate.[129]

Conclusions

It is clear that synchrotron radiation techniques have provided, and will continue to provide, important information to the medicinal chemist. Microprobe SRXRF has proven itself as a technique for providing unequalled information regarding the distribution of metal and metalloid-containing drugs in cells and tumours at subtoxic and therapeutic doses.[8,26,31-32,38,40-41,56] Targets such as the nucleus,[26,38] including the euchromatin[32] and heterochromatin[8] regions, nucleoli,[32,48,52] membranes, and mitochondria[52] can be identified as sites of localisation following studies of existing and potential therapeutic and diagnostic agents. The technique has been invaluable for confirming theories of drug actions (namely, the coordinative action of cisplatin and its analogues)[38-39] and for confirming concepts associated with the modes of action of designed therapeutics (namely, confirmation of drug penetration to the site of dense DNA).[8,40] In addition, microprobe SRXRF has been used to determine whether potential therapeutic agents remain intact[40] or dissociate following cell uptake.[41] The additional quantitative analysis of endogenous elements has become significant for probing changes to the homeostasis of the cells as exemplified in the studies of Ca changes associated with As uptake,[32] and intracellular K fluctuations following the uptake of Pt-Gd complexes.[40] Detection of subtle changes in the concentrations and distributions of endogenous cations or anions can provide invaluable information regarding apoptosis and other modes of drug action.

XAS has played a pivotal role in the structural analysis of therapeutic agents. It has been essential for confirming/elucidating the structure of newly prepared complexes,[85] and determining the fate of these complexes in biological solutions.[89] Not only has this given insight into the mechanisms of their action, but it has also helped to understand why some therapeutic agents might, or have shown, lower than expected efficacy.[85] The use of XAS for bulk cell analysis has provided insight into the metabolism of therapeutic agents and supplements[32,77,91] informing the medicinal chemist of expected products *in vivo* to be exploited for further design purposes or for progression to animal studies and human clinical trials.

Finally, the use of SR-FTIR microspectroscopy for studying the biomolecular effects of drugs *in vivo* and in cell culture has become prominent in the last 5 years with studies of anti-cancer drugs,[92,108-109,125] osteoporosis drugs,[102] and photodynamic therapeutics[111-112] showing distinguishable biomolecular changes. Issues associated with Mie scatter distortion of the spectra are being addressed,[92,122-124] and the technique is being critically assessed with a goal to using it for preclinical and clinical evaluation of drug candidates.[92,109,125] Clearly, major advances in the design of live cell sample holders will also aid in the study of therapeutic agents.[110,126-128]

In conclusion, it is anticipated that these synchrotron radiation spectroscopic techniques will play a major role in medicinal chemistry in the future especially as improvements in the instrumentation associated with the techniques evolves.

References

[1] M. W. Dong. *Modern HPLC for Practicing Scientists* **2006** (Wiley: Chinchester).

[2] L. H. J. Lajunen, P. Peramaki. *Advantages and Mutual Comparison of Atomic Spectroscopic Methods. Spectrochemical Analysis by Atomic Absorption and Emission.* **2004** pp. 324-327. (Royal Society of Chemistry: Cambridge).

[3] T. Paunesku, S. Vogt, J. Maser, B. Lai, G. Woloschak, *J. Cellular Biochem.* **2006**, *99*, 1489.

[4] C. J. Fahrni, *Curr. Opin. Chem. Biol.* **2007**, *11*, 121.

[5] D. B. Williams, C. B. Carter. *Transmission Electron Microscopy. A Textbook for Materials Science* **1996**. Plenum Press: New York.
[6] R. Jenkins. *X-Ray Fluorescence Spectrometry* (J. D. Winefordner) **1999**. (John Wiley and Sons: New York).
[7] K. L. Williams. *An Introduction to X-Ray Spectrometry* **1987** (Allen and Unwin: London).
[8] C. T. Dillon. *Synchrotron Radiation X-Ray Spectroscopy for Investigations of Intracellular Metallointercalators: X-Ray Fluorescence Imaging and X-Ray Absorption Spectroscopy.* In:. *Metallointercalators: Synthesis and Techniques to Probe Their Interactions with Biomolecules* (Ed. J. R. Adrich-Wright) **2011** (Springer-Verlag:Wein).
[9] F. Adams, K. Janssens, A. Snigirev, *J. Anal. At. Spectrom.* **1998**, *13*, 319.
[10] G. Botton. *Analytical Electron Microscopy.* In: *Science of Microscopy*. (P. W. Hawkes, J. C. H. Spence) **2007** pp. 273-405. (Springer: New York).
[11] G. J. F. Legge, A. P. Mazzolini, *Nucl Instr Meth Phys Res A* **1980**, *168*, 563.
[12] G. E. Ice, *X-Ray Spectrom.* **1997**, *26*, 315.
[13] P. Dhez, P. Chevallier, T. B. Lucatorto, C. Tarrio, *Rev. Sci. Instr.* **1999**, *70*, 1907.
[14] J. Kirz, D. Attwood. *X-Ray Data Booklet. Section 4.4 Zone Plates.* **2001** (Lawrence Berkeley National Laboratory) Available from: xdb.lbl.gov/Section4/Sec_4-4.html.
[15] A. Carmona, P. Cloetens, G. Deves, S. Bohic, R. Ortega, *J. Anal. At. Spectrom.* **2008**, *23*, 1083.
[16] R. Lobinski, C. Moulin, R. Ortega, *Biochimie* **2006**, *88*, 1591.
[17] R. Ortega, *Nucl. Instr. Meth. Phys. Res. B* **2005**, *231*, 218.
[18] F. van Lanevelde, R. D. Vis, *Anal. Chem.* **1991**, *63*, 2253.
[19] S. Bohic, A. Simionovici, R. Ortega, D. Heymann, C. Schroer, A. Snigirev, *Nucl. Instr. Meth. Phys. Res. B* **2001**, *181*, 728.
[20] M. Cholewa, C. Dillon, P. Lay, D. R. Phillips, T. Talarico, B. Lai, D. X. Blanc, Z. Barnea, Z. Cai, G. B. Deacon, P. Ilinski, D. Legnini, S. Rainone, G. Shea-McCarthy, A. P. J. Stampfi, L. K. Webster, W. Yun, *Nucl. Instr. Meth. Phys. Res. B* **2001**, *181*, 715.
[21] P. M. Bertsch, D. B. Hunter, *Chem. Rev.* **2001**, *101*, 1809.
[22] C. G. Ryan, B. E. Etschmann, S. Vogt, J. Maser, C.L. Harland, E. van Achterbergh, D. Legnini, *Nucl. Instr. Meth. Phys. Res. B* **2005**, *231*, 183.
[23] A. Thompson, D. Attwood, E. Gullikson, M. Howells, K.-J. Kim, J. Kirz, J. Kortright, I. Lindau, P. Pianetta, A. Robinson, J. Scofield, J. Underwood, D. Vaughan, H. Winick. *X-Ray Data Booklet* (Ed. C. Thompson, D. Vaughan) **2001**. Lawrence Berkeley National Laboratory: Berkeley, CA).
[24] J. B. Aitken, E. A. Carter, H. Eastgate, M. J. Hackett, H. H. Harris, A. Levina, Y.-C. Lee, C.-I. Chen, B. Lai, S. Vogt, P. A. Lay, *Radiation Phys. Chem.* **2010**, *79*, 176.
[25] Z. Cai, B. Lai, W. Yun, I. McNulty, A. Khounsary, J. Maser, P. Ilinski, D. Legnini, E. Trakhtenberg, S. Xu, B. Tieman, G. Wiemerslage, E. Gluskin, *Am. Inst. Phys. Conf. Proc.* **2000**, *521*, 31.
[26] P. Ilinski, B. Lai, Z. Cai, W. Yun, D. Legnini, T. Talarico, M. Cholewa, L. K. Webster, G. B. Deacon, S. Rainone, D. R. Phillips, A. P. J. Stampfl, *Cancer Res.* **2003**, *63*, 1776.
[27] E. Gullikson. *X-Ray Interactions with Matter.* **1995-2010** Center for X-ray Optics; Available from: http://henke.lbl.gov/optical_constants/.
[28] C. T. Dillon, P. A. Lay, B. J. Kennedy, A. P. J. Stampfl, Z. Cai, P. Ilinski, W. Rodrigues, D. G. Legnini, B. Lai, J. Maser, *J. Biol. Inorg. Chem.* **2002**, *7*, 640.

[29] E. A. Carter, B. S. Rayner, A. I. McLeod, L. E. Wu, C. P. Marshall, A. Levina, J. B. Aitken, P. K. Witting, B. Lai, Z. Cai, S. Vogt, Y.-C. Lee, C.-I. Chen, M. J. Tobin, H. H. Harris, P. A. Lay, *Mol. BioSyst.* **2010**, *6*, 1316.
[30] H. H. Harris, A. Levina, C. T. Dillon, I. Mulyani, B. Lai, Z. Cai, P. A. Lay, *J. Biol. Inorg. Chem.*, **2005**, *10*, 105.
[31] J. B. Waern, , H. H. Harris, , B. Lai, , Z. Cai, , M. M. Harding, , C. T. Dillon, *J. Biol. Inorg. Chem.* **2005**, *10*, 443.
[32] K. L. Munro, A. Mariana, A. Klavins, A. J. Foster, B. Lai, Z. Cai, S. Vogt, H. H. Harris, C. T. Dillon, *Chem. Res. Toxicol.* **2008**, *21*, 1760.
[33] M. D. Hall, C. T. Dillon, M. Zhang, P. Beale, Z. Cai, B. Lai, A. P. J. Stampfl, T. W. Hambley, *J. Biol. Inorg. Chem.* **2003**, *8*, 726.
[34] M. J. Hackett, J. A. McQuillan, F. El-Assaad, J. B. Aitken, A. Levina, D. D. Cohen, R. Siegele, E. A. Carter, G. E. Grau, N. H. Hunt, P. A. Lay, *Analyst* **2011**, *136*, 2941.
[35] R. McRae, B. Lai, S. Vogt, C. J. Fahrni, *J. Struct. Biol.* **2006**, *155*, 22.
[36] G. Liu, W. Huang, R. D. Moir, C. R. Vanderburg, B. Lai, Z. Peng, R. E. Tanzi, J. T. Rogers, X. Huang, *J. Struct. Biol.* **2006**, *155*, 45.
[37] J. J. Bozzola, L. D. Russell. *Electron Microscopy. Principles and Techniques for Biologists.* **1999** pp. 17-47 (Jones and Bartlett: Massachusetts).
[38] M. D. Hall, R. A. Alderden, M. Zhang, P. Beale, Z. Cai, B. Lai, A. P. J. Stampfl, T. W. Hambley, *J. Struct. Biol.* **2006**, *155*, 38.
[39] A. V. Klein, T. W. Hambley, *Chem. Rev.* **2009**, *109*, 4911.
[40] E. L. Crossley, J. B. Aitken, S. Vogt, H. H. Harris, L. M. Rendina, *Angew Chem. Int. Ed.* **2010**, *49*, 1231.
[41] E. L. Crossley, J. B. Aitken, S. Vogt, H. H. Harris, L. M. Rendina, *Aust. J. Chem.* **2011**, *64*, 253.
[42] M. H. Cohen, S. Hirschfeld, S. F. Honig, A. Ibrahim, J. R. Johnson, J. J. O'Leary, R. M. White, G. A. Williams, R. Pazdur, *The Oncologist* **2001**, *6*, 4.
[43] T. Bachleitner-Hofmann, M. Kees, H. Gisslinger, *Leuk. Lymph.* **2002**, *43*, 1535.
[44] D.-P. Lu, J.-Y. Qiu, B. Jiang, Q. Wang, K.-Y. Liu, Y.-R. Liu, S.-S. Chen, *Blood* **2002**, *99*, 3136.
[45] A. S. Don, O. Kisker, P. Dilda, N. Donoghue, X. Zhao, S. Decollogne, B. Creighton, E. Flynn, J. Folkman, P. J. Hogg, *Cancer Cell* **2003**, *3*, 497.
[46] I. Nicolis, P. Dacher, F. Guyon, P. Chevallier, E. Curis, S. Benazeth, *J. Trace Microprobe Tech.* **2002**, *20*, 565.
[47] I. Nicolis, E. Curis, P. Deschamps, S. Benazeth, *Biochimie* **2009**, *91*, 1260.
[48] K. L. Munro, C. T. Dillon, *Unpublished Results* **2010**.
[49] L. Yee-Chien, H. Haimei, *Mutagenesis* **1996**, *11*, 75.
[50] S. Orrenius, B. Zhivotovsky, P. Nicotera, *Nature Rev. Mol. Cell Biol.* **2003**, *4*, 552.
[51] P. Kopf-Maier, H. Kopf, *Angew Chem Int. Ed.* **1979**, *18*, 477.
[52] T. Paunesku, S. Vogt, B. Lai, J. Maser, N. Stojievi, K. T. Thurn, C. Osipo, H. Liu, D. Legnini, Z. Wang, C. Lee, G. E. Woloschak, *Nano Lett.* **2007**, *7*, 596.
[53] I. Imaz, M. Rubio-Martinex, L. Garcia-Fernandez, F. Carcia, D. Ruiz-Molina, J. Hernando, V. Puntes, D. Maspoch, *Chem. Commun.* **2010**, *46*, 4737.
[54] P. J. Endres, T. Paunesku, S. Vogt, T. J. Meade, G. Woloschak, *J. Am. Chem. Soc.* **2007**, *129*, 15760.
[55] P. A. Ali, A. F. Al-Hussany, C. A. Bennett, D. A. Hancock, A. M. El-Sharkawi, *Phys. Med. Biol.* **1998**, *43*, 2337.
[56] R. A. Alderden, H. R. Mellor, S. Modok, M. D. Hall, S. R. Sutton, M. G. Newville, R. Callaghan, T. W. Hambley, *J. Am. Chem. Soc.* **2007**, *129*, 13400.

[57] M. D. de Jonge, S. Vogt, *Curr. Opin. Struct. Biol.* **2010**, *20*, 606.
[58] J. E. Penner-Hahn, *Coord. Chem. Rev.* **2005**, *249*, 161.
[59] N. H. Zahler, *ACS Chem. Biol. 2010, 5*, 541.
[60] L. Finney, Y. Chishti, T. Khare, C. Giometti, A. Levina, P. A. Lay, S. Vogt, *ACS Chem. Biol.* **2010**, *5*, 577.
[61] I. Ascone, W. Meyer-Klaucke, L. Murphy, *J. Synch. Rad.* **2003**, *10*, 16.
[62] J. E. Penner-Hahn, *Coord. Chem. Rev.* **1999**, *190-192*, 1101.
[63] J. E. Penner-Hahn. *X-Ray Absorption Spectroscopy*. In: *Comprehensive Coordination Chemistry II.* (Ed. J. A. McCleverty, T. J. Meyer) **2004** pp. 159-86. Elsevier: Oxford.
[64] J. B. Aitken, A. Levina, P. A. Lay, *Curr. Topics Med. Chem.* **2011**, *11*, 553.
[65] A. Levina, R. S. Armstrong, P. A. Lay, *Coord. Chem. Rev.* **2005**, *249*, 141.
[66] C. T. Dillon, P. A. Lay, M. Cholewa, G. J. F. Legge, A. M. Bonin, T. J. Collins, K. L. Kostka, G. Shea-McCarthy, *Chem. Res. Toxicol.* **1997**, *10*, 533.
[67] A. Levina, H. H. Harris, P. A. Lay, *J. Am. Chem. Soc.* **2007**, *129*, 1065.
[68] C. Weeks, A. Levina, C. T. Dillon, P. Turner, R. R. Fenton, P. A. Lay, *Inorg. Chem.* **2004**, *43*, 7844.
[69] A. Levina, G. J. Foran, D. I. Pattison, P. A. Lay, *Angew Chem. Int. Ed.* **2004**, *43*, 462.
[70] R. Ortega, *J. Anal. At. Spectrom.* **2011**, *26*, 23.
[71] F. Jalilehvand, L. J. Laffin, *Inorg. Chem.* **2008**, *47*, 3248.
[72] E. C. Beret, K. Provost, D. Muller, E. S. Marcos, *J. Phys. Chem. B* **2009**, *113*, 12343.
[73] E. F. Molina, S. H. Pulcinelli, C. V. Santilli, S. Blanchandin, V. Briois, *J. Phys. Chem. B* **2010**, *2010*, 3461-6.
[74] M. D. Hall, G. J. Foran, M. Zhang, P. J. Beale, T. W. Hambley, *J. Am.Chem. Soc.* **2003**, *125*, 7524.
[75] H. L. Daly, M. D. Hall, T. W. Failes, M. Zhang, G. J. Foran, T. W. Hambley, *Aust. J. Chem.* **2011**, *64*, 273.
[76] I. Nicolis, P. Deschamps, E. Curis, O. Corriol, V. Acar, N. Zerrouk, J.-C. Chaumeil, F. Guyon, S. Benazeth, *J. Synch. Rad.* **2001**, *8*, 984.
[77] T. Bacquart, G. Deves, R. Ortega, *Environ. Res.* **2010**, *110*, 413.
[78] M. D. Hall, C. K. Underwood, T. W. Failes, G. J. Foran, T. W. Hambley, *Aust. J. Chem.* **2007**, *60*, 180.
[79] M. D. Hall, T. W. Failes, N. Yamomoto, T. W. Hambley, *Dalton Trans.* **2007**, 3983.
[80] P. D. Bonnitcha, M. D. Hall, C. K. Underwood, G. J. Foran, M. Zhang, P. J. Beale, T. W. Hambley, *J. Inorg. Biochem.* **2006**, *100*, 963.
[81] L. V. Liu, C. B. Bell, III, S. D. Wong, S. A. Wilson, Y. Kwak, M. S. Chow, J. Zhao, K. O. Hodgson, B. Hedman, E. I. Solomon, *Proc. Natl Acad. Sci.* **2010**, *107*, 22419.
[82] M. S. Walczak, K. Lawniczak-Jablonska, A. Wolska, M. Sikora, A. Sienkiewicz, L. Suarez, A. J. Kosar, M.-J. Bellemar, D. S. Bohle, *J. Phys. Chem.* **2011**, *115*, 4419.
[83] R. C. Elder, M. K. Eidsness, M. J. Heeg, K. G. Tepperman, C. F. Shaw III, N. Schaeffer, *ACS Symposium Series* **1983**, *209*, 385.
[84] L. Messori, A. Balerna, I. Ascone, C. Castellano, C. Gabbiani, A. Casini, C. Marchioni, G. Jaouen, A. Congiu Castellano, *J. Biol. Inorg. Chem.* **2011**, *16*, 491.
[85] J. E. Weder, T. W. Hambley, B. J. Kennedy, P. A. Lay, G. J. Foran, A. M. Rich, *Inorg. Chem.* **2001**, *40*, 1295.
[86] Q. Zhou, T. W. Hambley, B. J. Kennedy, P. A. Lay, *Inorg. Chem.* **2003**, *42*, 8557.
[87] A. Levina, A. Mitra, P. A. Lay, *Metallomics* **2009**, *1*, 458.

[88] I. Ascone, L. Messori, A. Casini, C. Gabbiani, A. Balerna, F. Dell'Unto, A. Congiu Castellano, *Inorg. Chem.* **2008**, *47*, 8629.
[89] M. Liu, Z. H. Lim, Y. Y. Gwee, A. Levina, P. A. Lay, *Angew Chem. Int. Ed.* **2010**, *49*, 1661.
[90] A. Nguyen, I. Mylyani, A. Levina, P. A. Lay, *Inorg. Chem.* **2008**, *47*, 4299.
[91] C. M. Weekley, J. B. Aitken, S. Vogt, L. A. Finney, D. J. Paterson, M. D. de Jonge, D. L. Howard, I. F. Musgrave, H. H. Harris, *Biochemistry* **2011**, *50*, 1641.
[92] K. R. Flower, I. Khalifa, P. Bassan, D. Demoulin, E. Jackson, N. P. Lockyer, A. T. McGown, P. Miles, L. Vaccari, P. Gardner, *Analyst* **2011**, *136*, 498.
[93] T. J. Harvey, E. Gazi, A. Henderson, R. D. Snook, N. W. Clark, M. Brown, P. Gardner, *Analyst* **2009**, *134*, 1083.
[94] M. J. Tobin, M. A. Chesters, J. M. Chalmers, F. J. M. Rutten, S. E. Fisher, I. M. Symonds, A. Hitchcock, R. Allibone, S. Dias-Gunasekara, *Faraday Discuss.* **2004**, *126*, 27.
[95] B. Rigas, S. Morgello, I. S. Goldman, P. T. T. Wong, *Proc. Natl Acad. Sci. USA* **1990**, *87*, 8140.
[96] K. R. Bambery, B. R. Wood, M. A. Quinn, D. McNaughton, *Aust. J. Chem.* **2004**, *37*, 1139.
[97] R. K. Dukor, M. N. Leibman, B. L. Johnson, *AIP Conf. Proc.* **1998**, *430*, 327.
[98] S. F. Chew, B. R. Wood, C. Kanaan, J. Browning, D. MacGregor, I. D. Davis, J. Cebon, B. D. Tait, D. McNaughton, *Tissue Antigens* **2007**, *69*, 252.
[99] D. Naumann, *Applied Spec. Rev.* **2001**, *36*, 239.
[100] A. Kretlow, Q. Wang, J. Kneipp, P. Lasch, M. Beekes, L. Miller, D. Naumann, *Biochem. Biophys. Acta* **2006**, *1758*, 948.
[101] L. M. Miller, Q. Wang, T. P. Telivala, R. J. Smith, A. Lanzirotti, J. Miklllossy, *J. Struct. Biol.* **2006**, *155*, 30.
[102] L. M. Miller, P. Dumas, N. Jamin, J.-L. Teillaud, J. Miklossy, L. Forro, *Rev. Sci. Instr.* **2002**, *73*, 1357.
[103] F. Severcan, G. Gorgulu, S. T. Gorgulu, T. Guray, *Anal. Biochem.* **2005**, *339*, 36.
[104] G. T. Webster, K. A. de Villiers, T. J. Egan, S. Deed, L. Tilley, M. J. Tobin, K. R. Bambery, D. McNaughton, B. R. Wood, *Anal. Chem.* **2009**, *81*, 2516.
[105] S.-Y. Lin, M.-J. Li, W.-T. Cheng, *Spectroscopy* **2007**, *21*, 1.
[106] P. Dumas, L. Miller, *Vib. Spectros.* **2003**, *32*, 3.
[107] C. Petibois, M. Piccinini, M. C. Guidi, A. Marcelli, *J. Synch. Rad.* **2010**, *17*, 1.
[108] F. Draux, P. Jeannesson, C. Gobinet, J. Sule-Suso, J. K. Pijanka, C. Sandt, P. Dumas, M. Manfait, G. D. Sockalingum, *Anal. Bioanal. Chem.* **2009**, *395*, 2293.
[109] G. Bellisola, M. Della Peruta, M. Vezzalini, E. Moratti, L. Vaccari, G. Birarda, M. Piccinini, G. Cinque, C. Sorio, *Analyst* **2010**, *135*, 3077.
[110] K. L. Munro, K. R. Bambery, E. A. Carter, L. Puskar, M. J. Tobin, B. Wood, C. T. Dillon, *Vib. Spectros.* **2010**, *53*, 39.
[111] S. Chio-Srichan, M. Refregiers, F. Jamme, S. Kascakova, V. Rouam, P. Dumas, *Biochem. Biophys. Acta* **2008**, *1780*, 854.
[112] A.-M. Mamoon, A. M. Gamal-Eldeen, M. E. Ruppel, R. J. Smith, T. Tsang, L. M. Miller, *Photodiagn. Photodyn. Ther.* **2009**, *6*, 105.
[113] A. Barth, *Biochem. Biophys. Acta* **2007**, *1767*, 1073.
[114] A. Pevsner, M. Diem, *Biopolymers* **2003**, *72*, 282.
[115] D. M. Blyer, H. Susi, *Biopolymers* **1986**, *25*, 469.
[116] Y. Wang, R. I. Boysen, B. R. Wood, M. Kansiz, D. McNaughton, M. T. W. Hearn, *Biopolymers* **2008**, *89*, 895.
[117] F. Gasparri, M. Muzio, *Biochem. J.* **2003**, *369*, 239.

[118] A. J. Bentley, T. Nakamura, A. Hammiche, H. M. Pollock, F. L. Martin, S. Kinoshita, N. J. Fullwood, *Molecular Vision* **2007**, *13*, 237.
[119] L. M. Miller, P. Dumas, *Biochim. Biophys. Acta* **2006**, *1758*, 846.
[120] E. A. Carter, K. K. Tam, R. S. Armstrong, P. A. Lay, *Biophys. Rev.* **2009**, *1*, 95.
[121] P. Bassan, A. Kohler, H. Martens, J. Lee, H. J. Byrne, P. Dumas, E. Gazi, M. Brown, N. Clarke, P. Gardner, *Analyst* **2010**, *135*, 268.
[122] B. Mohlenhoff, M. Romeo, M. Diem, B. R. Wood, *Biophys. J.* **2005**, *88*, 3635.
[123] P. Bassan, H. J. Byrne, F. Bonnier, J. Lee, P. Dumas, P. Gardner, *Analyst* **2009**, *134*, 1586.
[124] J. K. Pijanka, A. Kohler, Y. Yang, P. Dumas, S. Chio-Srichan, M. Manfait, G. D. Sockalingum, J. Sole-Suso, *Analyst* **2009**, *134*, 1176.
[125] K.-Z. Liu, L. Jia, S. M. Kelsey, A. C. Newland, H. H. Mantsch, *Apoptosis* **2001**, *6*, 269.
[126] M. J. Tobin, L. Puskar, R. L. Barber, E. C. Harvey, P. Heraud, B. R. Wood, K. R. Bambery, C. T. Dillon, K. L. Munro, *Vib. Spectros.* **2010**, *53*, 34.
[127] D. A. Moss, M. Keese, R. Pepperkok, *Vib. Spectros.* **2005**, *38*, 185.
[128] H.-Y. N. Holman, K. A. Bjornstad, M. P. McNamara, M. C. Martin, W. R. McKinney, E. A. Blakely, *J. Biomed. Optics* **2002**, *7*, 417.
[129] R. Y. Huang, L. M. Miller, C. S. Carlson, M. R. Chance, *Bone* **2002**, *30*, 492.

Figure Captions

Figure 1. Physical events associated with XRF spectroscopy that lead to the emission of characteristic X-rays. Allowed electronic transitions that give rise to characteristic X-ray lines are shown. E = Energy; BE = Binding Energy. Reprinted from: *Chapter 11. Synchrotron radiation X-Ray spectroscopy for investigations of intracellular metallointercalators: X-ray fluorescence imaging and X-ray absorption spectroscopy*, Dillon, C. T. in *Metallointercalators. Synthesis and techniques to probe their interactions with biomolecules*, (Ed. J. Aldrich-Wright) **2011,** Figure 11.1, p 275, Springer-Verlag/Wien, with kind permission from Springer Science and Business Media B.V.

Figure 2. Microprobe SR-XRF maps of P, S, Cl, K, Ca, Zn, Cu and As obtained from a thin-sectioned HepG2 cell that had been treated with arsenite (1 mM, 4 h). Scan dimensions: 20 × 20 μm, stepsize: 0.3 μm, dwell time: 3 s/pt. Reprinted with permission from: Munro, K. *et al.; Chem. Res. Toxicol.*, **2008**, *21*, 1760-1769. Copyright 2008 American Chemical Society.

Figure 3. Microprobe SRXRF elemental maps of A549 cells following treatment with : (A) cell media only; (B) $Ni(phen)_2(dppz)]^{2+}$ (960 μM), or (C) [Pt(56MESS)] (490 μM). The elements are specified at the bottom of each column. Operating conditions include: Beam energy = 11.9 keV, Beam size = 0.2 μm × 0.15 μm; Stepsize = 0.3 μm; Dwell time = 3 s/pt and Scan dimensions (H × V) = (A) 9 μm × 10 μm; (B) 14 μm × 14 μm (C) 10 μm × 10 μm. Reprinted from: *Chapter 11. Synchrotron radiation X-Ray spectroscopy for investigations of intracellular metallointercalators: X-ray fluorescence imaging and X-ray absorption spectroscopy*, Dillon, C. T. in *Metallointercalators. Synthesis and techniques to probe their interactions with biomolecules*, (Ed. J. Aldrich-Wright) **2011,** Figure 11.5, p 287, Springer-Verlag/Wien, with kind permission from Springer Science and Business Media B.V.

Figure 4. Experimental setup employed for XAS data collection. Reprinted from: *Chapter 11. Synchrotron radiation X-Ray spectroscopy for investigations of intracellular metallointercalators: X-ray fluorescence imaging and X-ray absorption spectroscopy*, Dillon, C. T. in *Metallointercalators. Synthesis and techniques to probe their interactions with biomolecules*, (Ed. J. Aldrich-Wright) **2011,** Figure 11.7, p 293, Springer-Verlag/Wien, with kind permission from Springer Science and Business Media B.V.

Figure 5. Typical XAS spectrum defining the XANES and EXAFS regions and showing typical spectral features. Reprinted from: *Chapter 11. Synchrotron radiation X-Ray spectroscopy for investigations of intracellular metallointercalators: X-ray fluorescence imaging and X-ray absorption spectroscopy*, Dillon, C. T. in *Metallointercalators. Synthesis and techniques to probe their interactions with biomolecules*, (Ed. J. Aldrich-Wright) **2011,** Figure 11.6, p 290, Springer-Verlag/Wien, with kind permission from Springer Science and Business Media B.V.

Figure 6. Live cell sample holder (**A-C**) including the two spacers (**A** and **C**) and the entire holder (**B**). Resultant live cell spectra are shown (**D**) and include SR-FTIR averaged spectra from HL60 control cells (40 min, ─, n=23) and HL60 cells treated with 100 µM arsenite: 40 min (─, n=20), 60 min (─, n=20), 100 min (─, n=18) and 120 min (─ , n=15).[92,107]

Figure 1

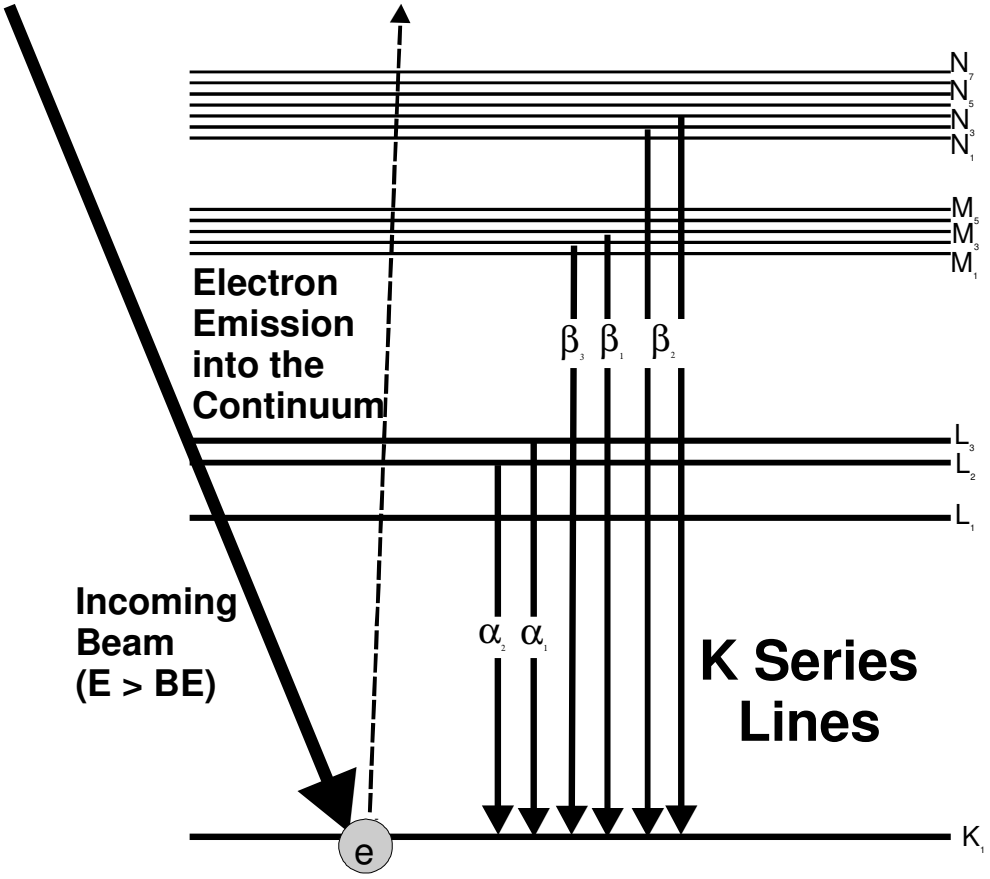
N7
N5
N3
N1
M5
M3
M1
Electron
Emission
into the
Continuum
β3 β1 β2
L3
L2
L1
Incoming
Beam
(E > BE)
α2 α1
K Series
Lines
e
K1

Figure 2

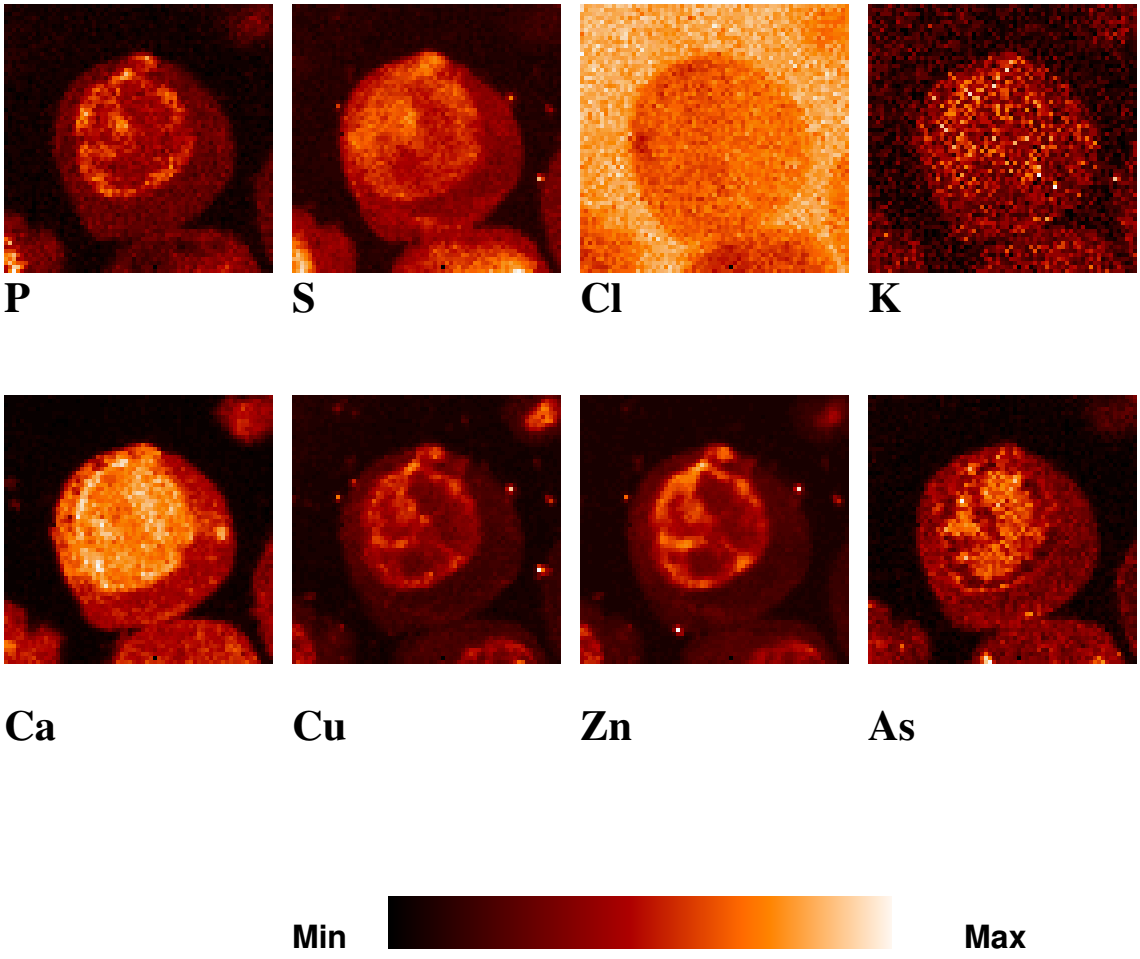

Figure 3

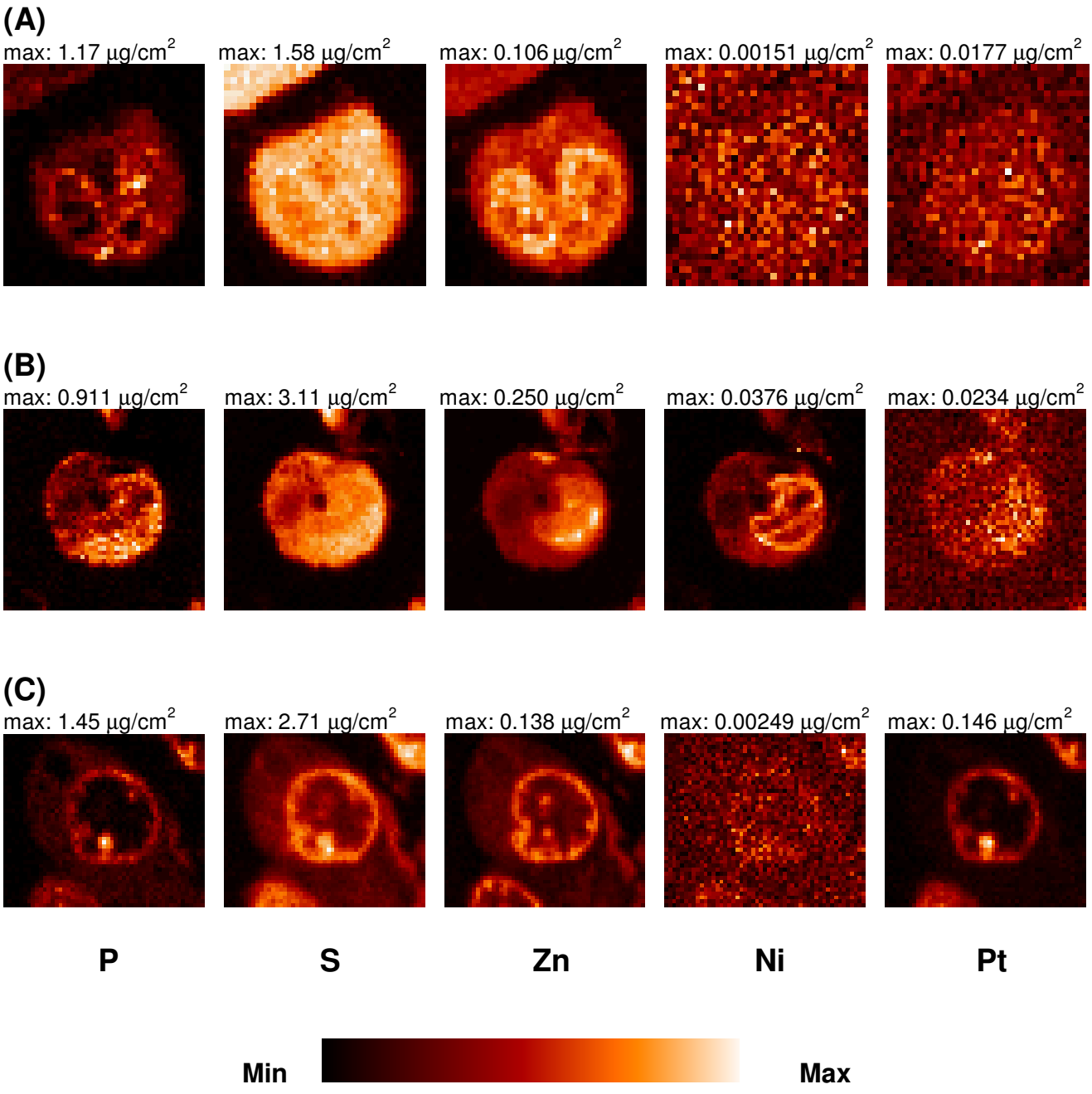
(A)
max: 1.17 µg/cm2
max: 1.58 µg/cm2
max: 0.106 µg/cm2
max: 0.00151 µg/cm2
max: 0.0177 µg/cm2
(B)
max: 0.911 µg/cm2
max: 3.11 µg/cm2
max: 0.250 µg/cm2
max: 0.0376 µg/cm2
max: 0.0234 µg/cm2
(C)
max: 1.45 µg/cm2
max: 2.71 µg/cm2
max: 0.138 µg/cm2
max: 0.00249 µg/cm2
max: 0.146 µg/cm2
P
S
Zn
Ni
Pt
Min
Max

Figure 4

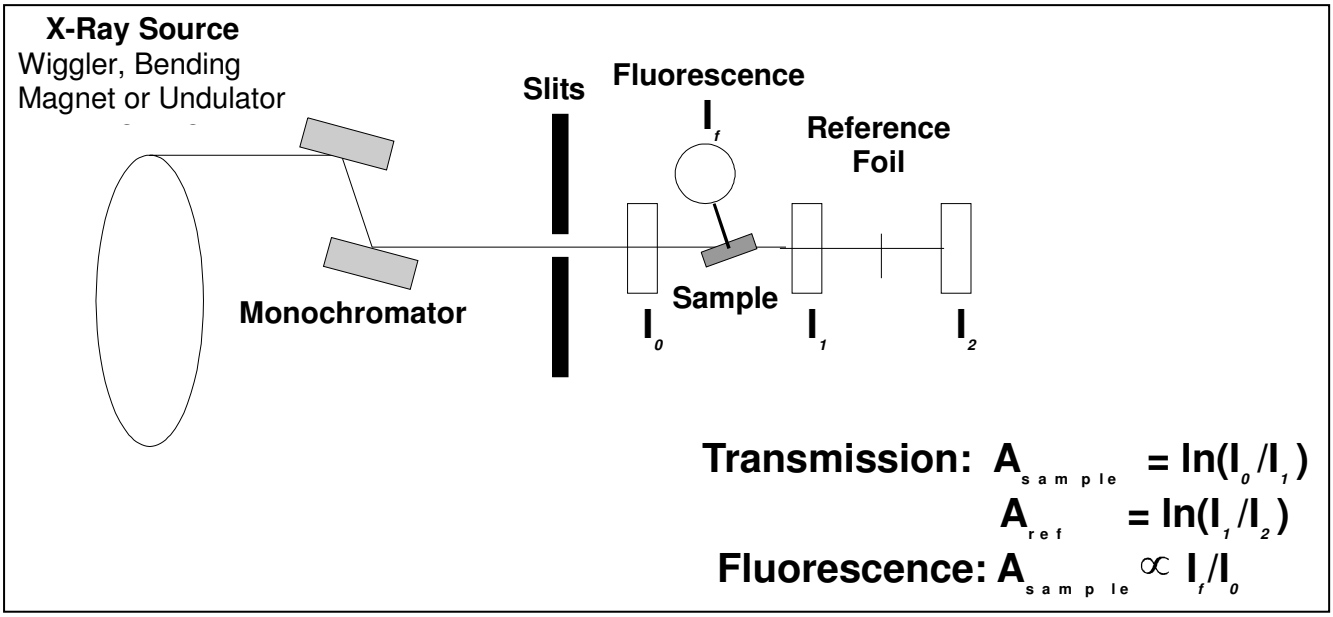
X-Ray Source
Wiggler, Bending
Magnet or Undulator
Slits
Fluorescence
I_f
Reference
Foil
Monochromator
Sample
I_0
I_1
I_2
Transmission: $A_{sample} = \ln(I_0/I_1)$
$A_{ref} = \ln(I_1/I_2)$
Fluorescence: $A_{sample} \propto I_f/I_0$

Figure 5

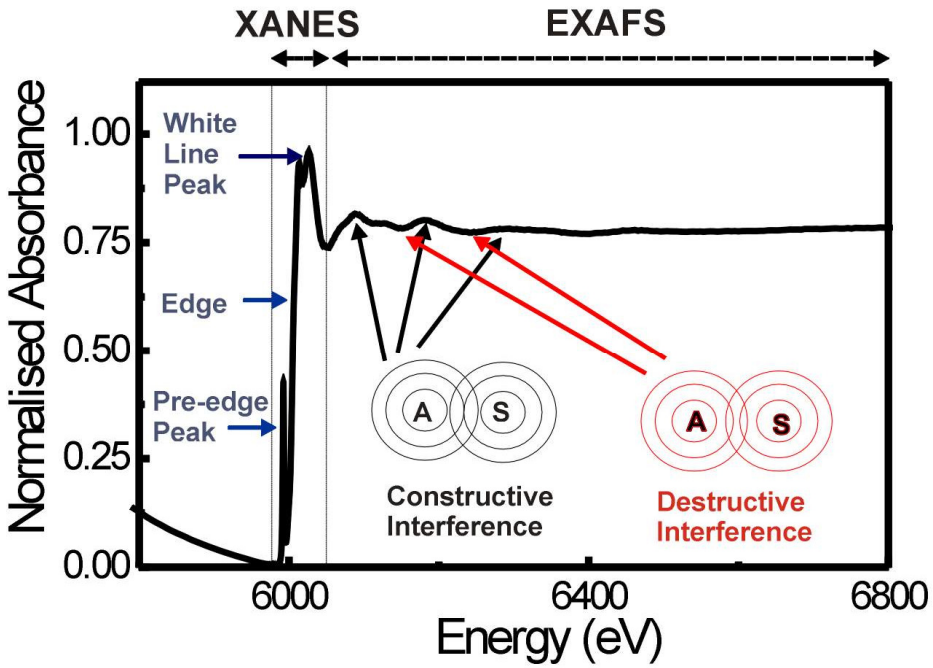
XANES
EXAFS
Normalised Absorbance
1.00
0.75
0.50
0.25
0.00
White Line Peak
Edge
Pre-edge Peak
A
S
Constructive Interference
A
S
Destructive Interference
6000
6400
6800
Energy (eV)

Figure 6

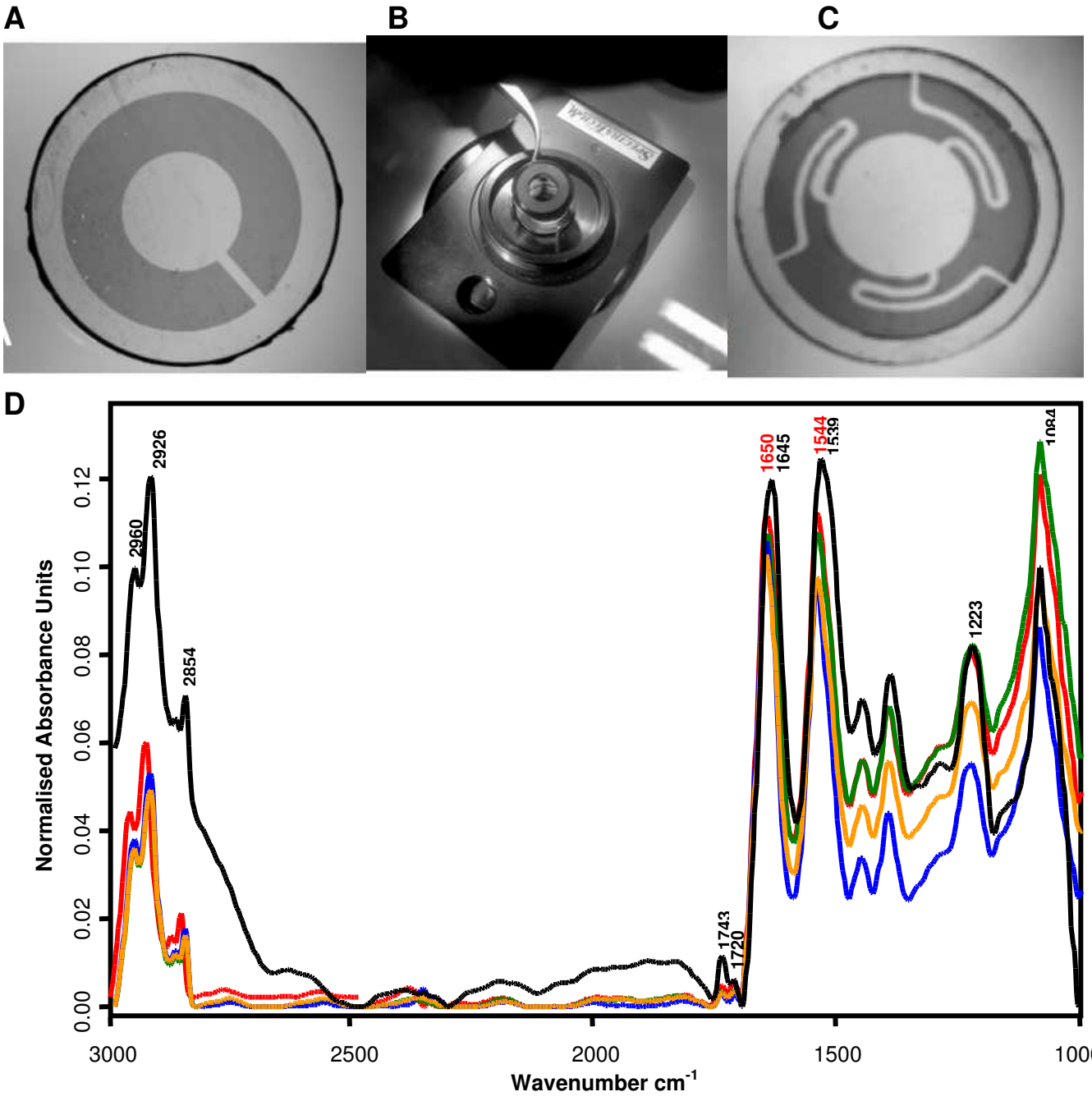
A
B
C
D
Normalised Absorbance Units
0.00
0.02
0.04
0.06
0.08
0.10
0.12
2926
2960
2854
1650
1645
1544
1539
1743
1720
1223
1084
3000
2500
2000
1500
1000
Wavenumber cm-1